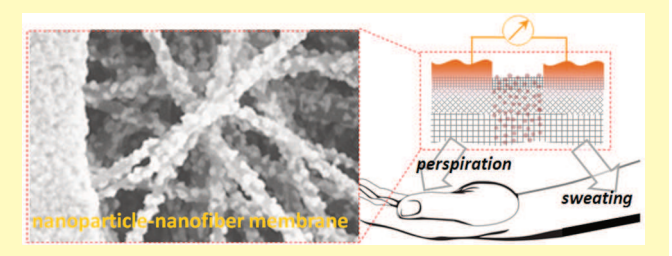


Nanoparticle—Nanofibrous Membranes as Scaffolds for Flexible **Sweat Sensors**

Ning Kang,[†] Fang Lin,[†] Wei Zhao,[†] Jack P. Lombardi,[‡] Mihdhar Almihdhar,[§] Kai Liu,[§] Shan Yan,[†] Juhee Kim,[†] Jin Luo,[†] Benjamin S. Hsiao,[§] Mark Poliks,[‡] and Chuan-Jian Zhong^{*,†}

Supporting Information

ABSTRACT: The ability to tune the sensing properties with nanostructured materials in a flexible scaffold is essential for constructing highly sensitive and wearable sensors or biosensors. Here we demonstrate a novel class of nanoparticle—nanofibrous membranes as a tunable interfacial scaffolds for flexible sweat sensors by assembling gold nanoparticles (Au NPs) in a multilayered fibrous membrane consisting of cellulose nanofiber (CN) top layer (fiber diameter 5 nm), electrospun polyacrylonitrile (PAN) nanofibrous midlayer (fiber diameter 150 nm), and



nonwoven polyethyleneterephthalate (PET) fibrous support layer (fiber diameter 20 µm) through interparticle molecular/ polymeric linkages and nanoparticle-nanofibrous interactions. One strategy involves 11-mercaptoundecanoic acid (MUA) as a molecular linker having hydrogen-bonding groups for interlinking alkanethiolate-capped Au NPs, and the other features poly(diallyldimethylammonium) (PDA) as a matrix with positively changed groups for anchoring negative-charge capped Au NPs. Impedance measurements of the nanocomposite membrane (Au NPs/CN/PAN/PET) as a scaffold on chemiresistor-type platforms have demonstrated the viability of detecting ionic species in solutions with dissolved salts with different cations and changes of relative humidity in gas phase. This type of nanoparticle-nanofibrous scaffold is further demonstrated as a flexible sensor strip for detecting changes in sweating and perspiration for volunteers before and after exercise. The sensitivity of the electrical responses depends on the nature of molecular interactions in the nanocomposite materials. Implications of the findings for potential applications of the flexible nanocomposite scaffolds in developing wearable sweat sensors are also discussed.

KEYWORDS: nanoparticle—nanofibrous membrane, nanocomposite scaffolds, gold nanoparticle assembly, cellulose nanofiber, electrospun polyacrylonitrile, sweat, wearable sensors

 \mathbf{S} weating is primarily used to regulate body temperature by cooling the body down with secretion of water. The inability of human body to sweat properly is potentially harmful, and a complete absence of sweating (anhidrosis) or sweating less than normal (hypohidrosis) is an abnormal lack of sweat in response to heat, which is also one of the symptoms of some genetic diseases. ¹⁻⁴ As such, monitoring of the moisture levels from perspiration provides useful information for assessing the physical conditions, especially for people exposed to high temperature or experiencing long time exercise who face the risk of dehydration.^{5,6} The fact that sweat contains abundant medical information has been an important driving force for the increasing interests in developing wearable sweat sensors.^{7–16} In addition to moisture, sweat is also rich with ions such as sodium, potassium and chlorine ranging from 10 to 80 mM. 17,18 Monitoring the saltiness thus provides further useful information. Moreover, sweat may also contain biomarkers related to metabolites of the human body, e.g., glucose, lactate, and uric acid. ^{19,20} While progress has been made in developing sweat sensors, ^{21,22} key challenges remain, including lack of multifunctionality, biocompatibility, and flexibility in some

monitoring conditions, high cost in manufacturing, and insufficient sensitivity and selectivity, calling for breakthroughs in materials design and fabrication.

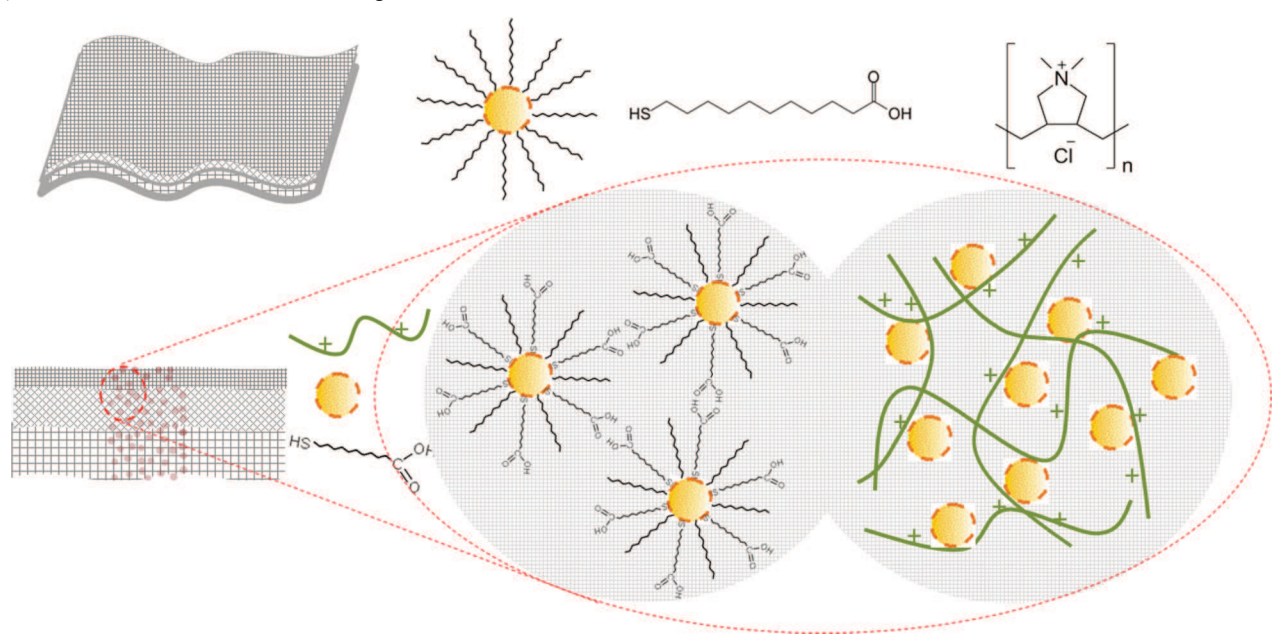
In comparison with traditional 2D sensing materials in most previous studies of sweat sensors, a 3D scaffold could offer intriguing opportunities to address some of the current challenges. Especially, the incorporation of nanoparticle assembly into nanofibrous membranes (NM) represents a new pathway for constructing flexible sensors with tunable electrical properties. One important classification of nanofibrous membrane consists of three-layered structures including a cellulose nanofiber (CN) top layer (fiber diameter around 5 nm), electrospun polyacrylonitrile (PAN) midlayer (fiber diameter around 150 nm), and nonwoven polyethyleneterephthalate (PET) substrate layer (fiber diameter around 20 μ m), featuring a combination of nano- and microporosities with

Received: July 2, 2016 Accepted: August 3, 2016 Published: August 8, 2016

[†]Department of Chemistry, and [‡]System Science and Industrial Engineering, State University of New York at Binghamton, Binghamton, New York 13902, United States

[§]Department of Chemistry, Stony Brook University, Stony Brook, New York 11794, United States

Scheme 1. Illustrations of the Nanofibrous Membrane (NM), Gold Nanoparticles and Molecular/Polymeric Linkers (Top Panel), and the Nanocomposite Scaffolds by Molecularly-Mediated Hydrogen-Bonding Linkages of Au NPs (M-NPs) or Polymer-Mediated Electrostatic Linkages of Au NPs (P-NPs) in the NM (Bottom Panel)



extremely high surface to volume ratio. 23-25 To impart electrically responsible function to the nanofibrous membrane toward chemical sensing, molecularly mediated nanoparticles assembly and thin film²⁶⁻²⁹ offer highly tunable molecular interactions and electrical properties. Here we demonstrate a novel class of nanocomposite scaffolds structured by assembling gold nanoparticles (Au NPs) in a flexible multilayered nanofibrous membrane through interactions involving molecular linkage and electrostatic binding, which is to our knowledge the first example of this kind in terms of the specific architecture. The CN (thickness < 2 µm) /PAN (thickness $\sim 40 \ \mu m$) /PET (thickness $\sim 100 \ \mu m$) three-layer membrane was utilized in combination with assemblies of Au NPs with different nanoparticle-nanofibrous interactions. One involves 11-mercaptoundecanoic acid (MUA) as a molecular linker having hydrogen-bonding groups for interlinking alkanethiolate-capped Au NPs, and the other features poly-(diallyldimethylammonium) (PDA) as a matrix with positively charged groups for anchoring negative-charge capped Au NPs. Results will be shown for the detection of chemical species relevant to sweating or perspiration such as moisture and ionic species, demonstrating the viability of potential applications of a new class of nanoparticle-nanofibrous membranes in wearable sweat sensors.

■ EXPERIMENTAL SECTION

Chemicals and Synthesis of Gold Nanoparticles. Hydrogen tetrachloroaurate trihydrate (99%), tetraoctylammonium bromide (99%), decanethiol (DT, 96%), sodium borohydride (99%), 11-mercaptoundecanoic acid (MUA, 95%), (poly)diallyldimethylammonium (PDA) (20%), sodium acrylate, sodium chloride (NaCl), potassium chloride (KCl), lithium chloride (LiCl), and graphite powders were purchased from Aldrich. Solvents included hexane (Hx, 99.9%) and toluene (Tl, 99%) from Fisher, and ethanol (99.9%) from Aldrich. Water was purified with a Millipore Milli-Q water system. 2,2,6,6-Tetramethylpiperidinooxy (TEMPO, 98%) was purchased from Acros. Sodium hypochlorite (NaClO solution, available chlorine 7–10%) was purchased from Sigma-Aldrich. Sodium bromide (NaBr) was obtained

from Fisher Scientific Company. Polyacrylonitrile (PAN) having an average molecular weight (Mw) of 150 kDa was purchased from Sigma-Aldrich. Poly(ethylene terephthalate) nonwoven substrate (PET microfilter FO2413 with an average fiber diameter of about 30 μ m) for the membrane support was provided by Freudenberg Nonwovens (Hopkinsville, KY).

Gold nanoparticles of 2 nm (Au_{2nm}) capped with decanethiolate (DT) monolayer shells were synthesized by two-phase reduction of AuCl₄ $^-$ according to Brust's two-phase protocol³⁰ and a synthetic modification. DT-capped gold nanoparticles of 7.1 \pm 1.0 nm diameter were synthesized from a thermally activated processing of Au_{2nm} nanoparticles developed in our laboratory. Briefly, the solution containing the as-synthesized DT-Au_{2nm} nanoparticles was heated at 150 °C to produce larger-sized Au nanoparticles. Details for morphology and size distribution can be found in previous reports. Acrylate-capped gold nanoparticles 42 nm (42.2 \pm 6.9 nm) and 70 nm (70.6 \pm 2.0 nm) were prepared by a seeded aggregative growth method developed in our laboratory. Briefly, the synthesis involves reacting mixture of Au seeds (30 nm) and HAuCl₄ under controlled concentrations of the reducing and capping agents, which produced acrylate-capped Au NPs of >30 nm. Details for morphology and size distribution can be found in previous reports. 34

Preparation of Nanofibrous Membranes. Ultrafine cellulose nanofibers were prepared by the following procedure. In brief, 10 g of wood pulps (Biofloc 96 supplied by the Tembec Tartas factory in France) was dispersed in 192 g of water. NaBr (0.2 g) and TEMPO (0.04 g) were subsequently dissolved in the suspension. Then 30 g of 10–15% NaClO aqueous solution was added to start this reaction. The pH value of the system was adjusted in the range of 10.0–10.3 by adding sodium hydroxide (NaOH) aqueous solution (0.5 mol/L). After 24 h, the reaction was stopped by adding ethanol (10 mL). The oxidized cellulose product was purified by dialysis process. The resulting cellulose slurry was dispersed in 100 g of water by using a homogenizer (Cole Parmer, VCX-400) for 5 min. The CN concentration was determined by using a Total Organic Carbon analyzer (TOC-500, Shi-madzu Corporation).

To prepare electrospun PAN/PET substrate, PAN was dissolved in DMF at $60\,^{\circ}\text{C}$ for 2 days until the mixture became a homogeneous solution (the solution concentration was 8 wt %). The homogeneous PAN solution was electrospun onto the nonwoven PET substrate under a high electrical voltage of 20 kV. The flow rate during this

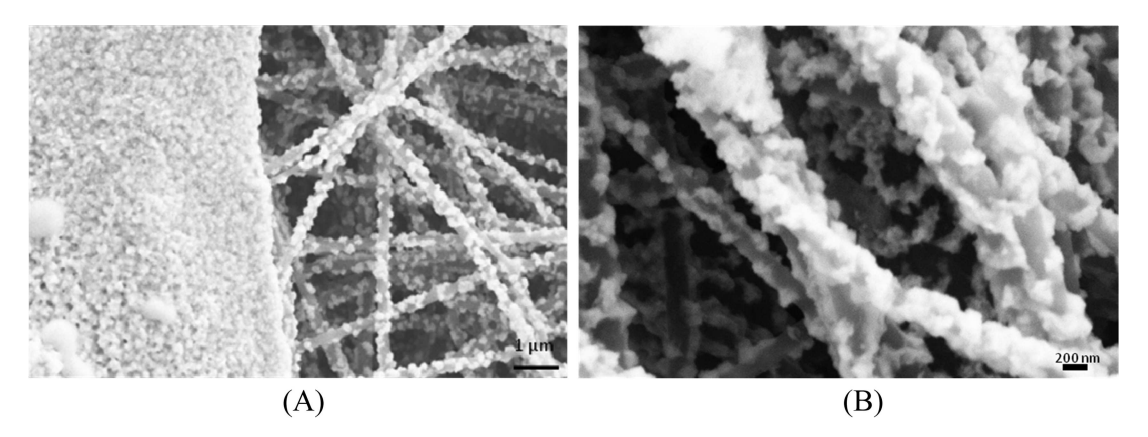
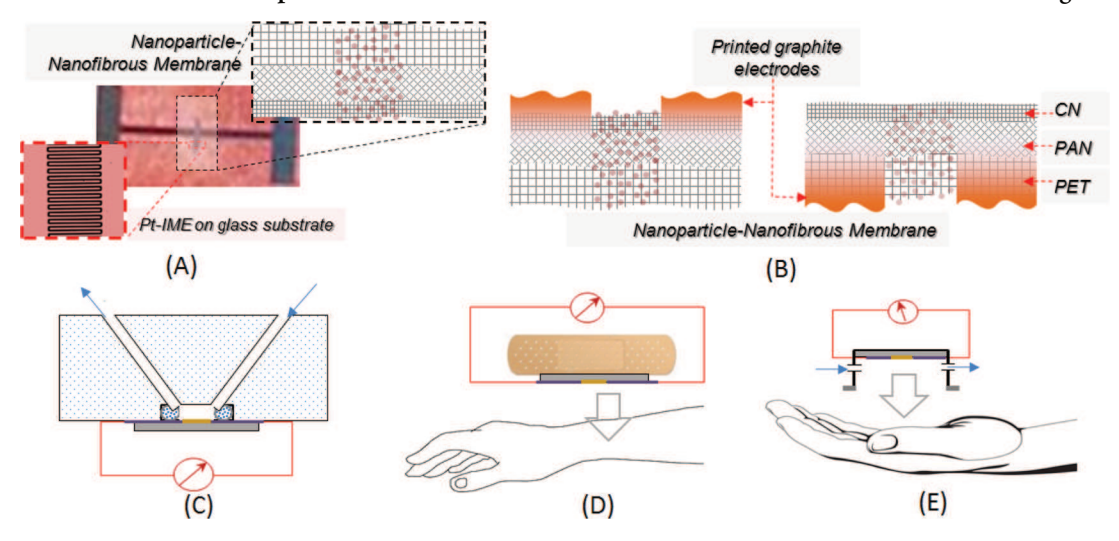


Figure 1. SEM images of MUA-mediated assembly of DT-capped 7 nm Au NPs (M-NPs/NM) in CN/PAN/PET membrane: (A) nanoparticles on the CN and PAN fibers and (B) magnified image of the nanoparticles on the PAN fibers.

Scheme 2. Illustrations of the Nanoparticle-Nanofibrous Membrane Sensor Device and Measurement Configurations^a



"(A) Membrane being placed on top of a Pt IME device; (B) membrane with graphite printed electrodes (G-PE) in which G-PE is on either the CN or PET side (from left to right); (C) manifold with embedded flow channels and a sample-holding plate with electrical leads for impedance measurement under controlled liquid or gas flow; (D) patch with a thin nonwoven scaffold between the membrane and the wrist skin for sweat detection; and (E) mini-compartment where the NM is placed above the palm for perspiration detection.

electrospinning operation was 16 μ L/min and the inner diameter of the spinneret was 0.7 mm. The working distance between the spinneret and the collector was 10 cm. The average fiber diameter of the electrospun nanofiber estimated from the SEM image was 150 \pm 10 nm.

To complete the three-layered fibrous membrane containing the ultrafine cellulose nanofiber top layer, the electrospun PAN/PET substrate was first immersed in an acidic aqueous solution (pH = 2). The cellulose nanofiber aqueous suspension (0.05 wt%) was subsequently cast on top of the electrospun PAN nanofibrous scaffold. The low pH value was used to gel the cellulose nanofiber suspension, thus preventing the penetration of cellulose nanofibers into the electrospun scaffold. The barrier layer thickness was controlled by the gap of the casting knife. After coating, the resulting membrane was dried at room temperature and forms a uniform coating layer of CN.

Preparation of Nanoparticle–Nanofibrous Membranes. For the assembly of MUA-linked DT-capped Au NPs in NM (M-NPs/NM), typically a controlled volume (e.g., 2 μ L) of MUA mediated Au NPs solution (7.1 × 10¹⁴ NPs/mL) was directly deposited in the nanofibrous membrane (NM). For the assembly of PDA-linked acrylate-capped Au NPs in the NM (P-NPs/NM), a controlled volume of 10× concentrated acrylate-capped 70 nm Au NPs (5.0 × 10¹¹ NPs/mL), or 2× concentrated 42 nm NPs (2.7 × 10¹³ NPs/mL), was first mixed with PDA solution (0.4 M) by sonication for 10 min. A

controlled volume (2 μ L) of the solution was then deposited in the NM, followed by further annealing at room temperature for at least 1 h before use.

Instrumentation and Measurements. Electrochemical impedance spectroscopic (EIS) measurements were performed on a SP-150 single-channel potentiostat (Biologic). The spectra were recorded at open circuit in a frequency range from 100 kHz to 0.1 Hz.

Transmission electron microscopy (TEM) was employed to determine the morphology of the nanoparticles. TEM was performed on a JEOL JEM-ARM200F instrument operated at 200 kV with a spherical aberration corrector. The nanoparticle samples were suspended in hexane or water before drop casting on a carbon-coated copper grid. The samples were then dried by evaporation in ambient atmosphere.

Scanning electron microscopy (SEM) images of the nanofibrous membrane and nanocomposite were performed with a LEO-1550 (Carl Zeiss) field emission scanning electron microscope. The membrane samples were mounted on a sample holder. It was then followed by carbon-coating with a sputter coater.

■ RESULTS AND DISCUSSION

General Characteristics of Nanocomposite Membranes and Devices. As illustrated in Scheme 1, two

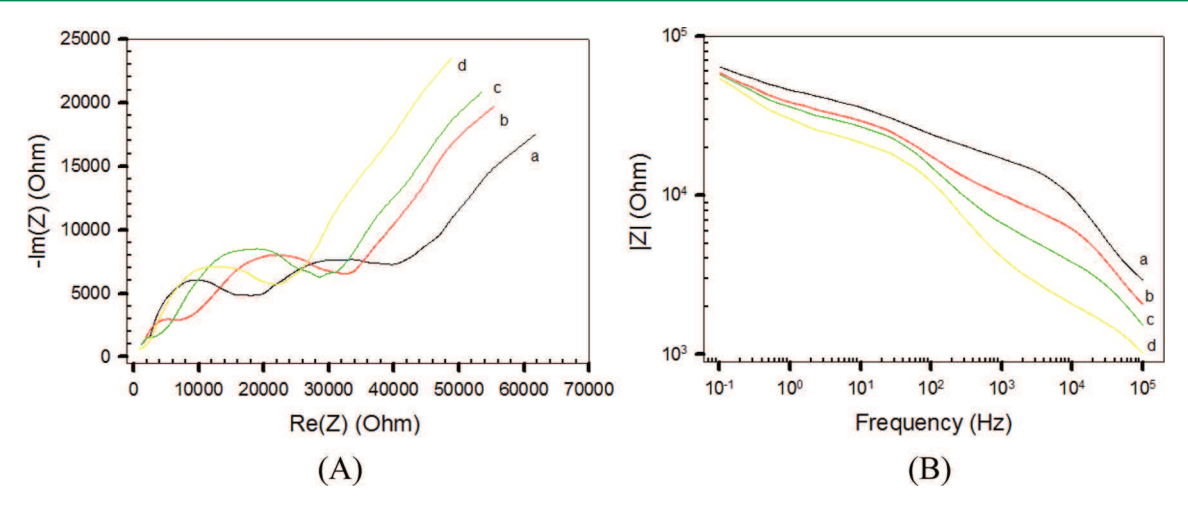


Figure 2. (A) Nyquist and (B) Bode impedance plots of MUA-AuNPs/CN/PAN/PET NM placed on top of a Pt interdigitated IME device in solutions of Na⁺ with different concentration (5 (a), 20 (b), 40 (c), and 80 mM (d)).

pathways have been explored for assembling Au NPs in the three-layered CN/PAN/PET membrane by either molecular linkers or polymeric electrostatic interactions. One pathway involves a molecular linker MUA, which forms molecularly mediated thin-film assembly of Au NPs (M-NPs) via hydrogen bonding. In this case, the interaction between the nanoparticle assemblies and the nanofibers feature mainly hydrophobic interactions. The other pathway involves polymeric linker PDA, which forms polymer-mediated thin film assembly of Au NPs (P-NPs) in the membrane via electrostatic interactions. In this case, the polymeric structure provides an adhesive force between the nanoparticle assemblies and the nanofibers.

Gold nanoparticles of different sizes and hydrophilicity characteristics were studied for their assembly in the nanofibrous membranes, including hydrophobic DT-capped Au NPs and hydrophilic acrylate-capped Au NPs (Figure S1). While the DT-capped Au NPs (7 nm) and acrylate-capped Au NPs (42 nm, or 70 nm) feature highly monodispersed sizes, the nanofibrous membrane features a three-layer CN/PAN/PET structure (Figure S2A-C). As shown in Figure 1 for the MUAlinked DT-capped 7 nm sized Au NPs in the NM (M-NPs/ NM), the nanoparticles are well distributed on the surface of the CN layer and along the PAN fibers (see also Figure S2D). Similar assemblies were also observed for PDA-linked acrylatecapped 42 or 70 nm Au NPs (P-NPs/NM) in the NM, but with a less even distribution on the fibers and a certain degree of aggregation at cross-fiber junctions (Figure S2E,F). The fact that M-NPs/NM shows a much better dispersion of NPs along the fibers than that for the P-NPs/NM indicates that the assembly depends on the surface properties of the nanoparticles and the solvent used for the assembly. Au NPs of different sizes have been assembled in the NM, but this report focuses on selected examples for the exploration of sensing properties.

The M-NPs/NM, i.e., MUA-AuNPs/CN/PAN/PET, features largely hydrophobic network with partial hydrophilic domains (i.e., the region of hydrogen-bonding of carboxylic acid groups). In contrast, the P-NPs/NM, i.e., PDA-AuNPs/CN/PAN/PET, features largely hydrophilic network with partial hydrophobic polymer backbone structure. Both nanocomposite membranes were studied as resistance- or conductance-responsive scaffolds on chemiresistor-type platform via two different approaches. The first involves placing the NPs/NM on top of a prefabricated Pt-interdigitated micro-

electrode (Pt-IME) device (Scheme 2A), whereas the second involves configuring the NPs/NM in between a printed pair of graphite electrodes on CN or PET sides of the membrane with a controlled gap (0.5–1.0 mm) (Scheme 2B). In each approach, the electrical responses to the analytes such as ions in a solution or moisture change in a gas atmosphere were measured by impedance spectroscopy. As illustrated in Scheme 2C–E, the measurements were performed in a manifold where the NM is sandwiched between manifold with embedded flow channels and a sample-holding plate with electrical leads (C), a patch where the NM is placed against the wrist skin to detect sweat (D) (see Figure S6A), or a mini-compartment where the NM is placed above the skin to detect perspiration from the palm (E) (see Figure S6B).

Ideally, the above chemiresistor-type device can be represented by two equivalent circuit models featuring the nanoparticle—nanofibrous membrane with two-electrode configurations (see Scheme S1). One consists of two double layer capacitors (capacitance near the surface of an electrode, $C_{\rm dl}$), one for each set of the electrodes, connected in series with a parallel combination of a membrane resistor ($R_{\rm m}$) and a membrane dielectric capacitor ($C_{\rm m}$), and all of them in parallel with a parasitic capacitor. The other model consists of two double layer capacitors ($C_{\rm dl}$), connected in series with a medium resistor ($R_{\rm s}$), and a dielectric capacitor ($C_{\rm di}$).

Detection of Salts Dissolved in Water and from **Sweat.** Detection of Salts in Water. In this section, we first discuss the results of the M-NPs/NM scaffolds. With a sensor device of M-AuNPs/CN/PAN/PET on Pt-IME (CN facing Pt-IME, Scheme 2A) placed in the test manifold (Scheme 2C), solution samples of K+, Na+, and Li+ with a common anion (Cl⁻), prepared by dissolving KCl, NaCl or LiCl in aqueous solutions with controlled concentrations, were introduced by a flow controller. Figure 2A shows a representative set of Nyquist impedance plots of solutions with different Na⁺ concentrations. Similar results have also been obtained from samples of K⁺ or Li⁺ solutions. The semicircle characteristic of the charge transfer region and the slope characteristic of the mass transfer region show clear variations with the concentration of ions. In Figure 2B, the data are plotted in Bode impedance, which clearly reveals that absolute impedance |Z| depends on the Na⁺ concentration.

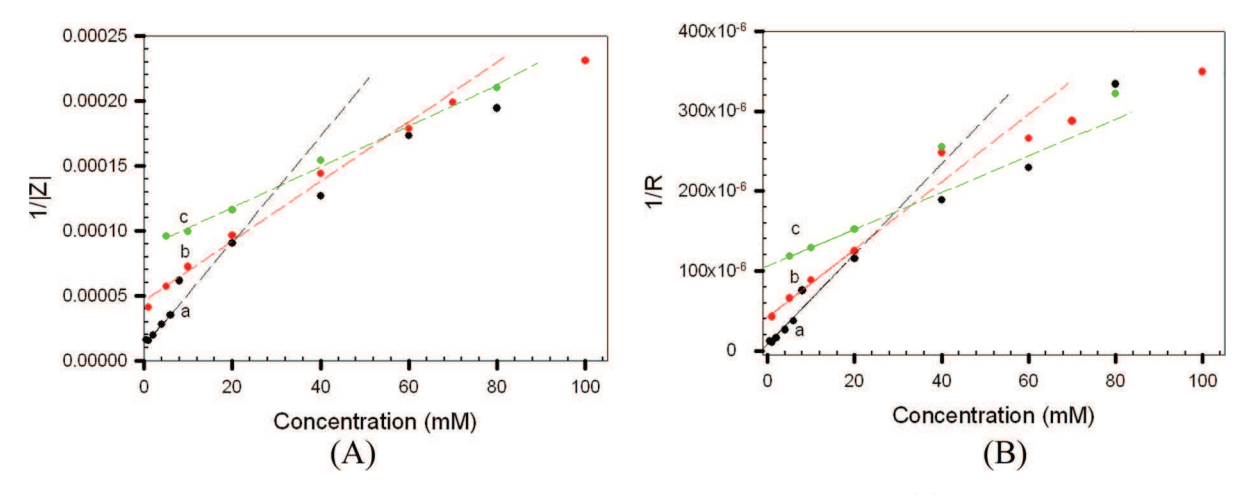


Figure 3. Plots of impedance and resistance values from Bode impedance and Nyquist impedance plots. (A) 1/|Z| vs concentration curves obtained from Bode impedance plots at 1 kHz. (B) 1/R values obtained by semicircle fit to Nyquist impedance plots with MUA-AuNPs/CN/PAN/PET NM on Pt-IME in solutions of K^+ (a), Na^+ (b), and Li^+ (c) as a function of concentration.

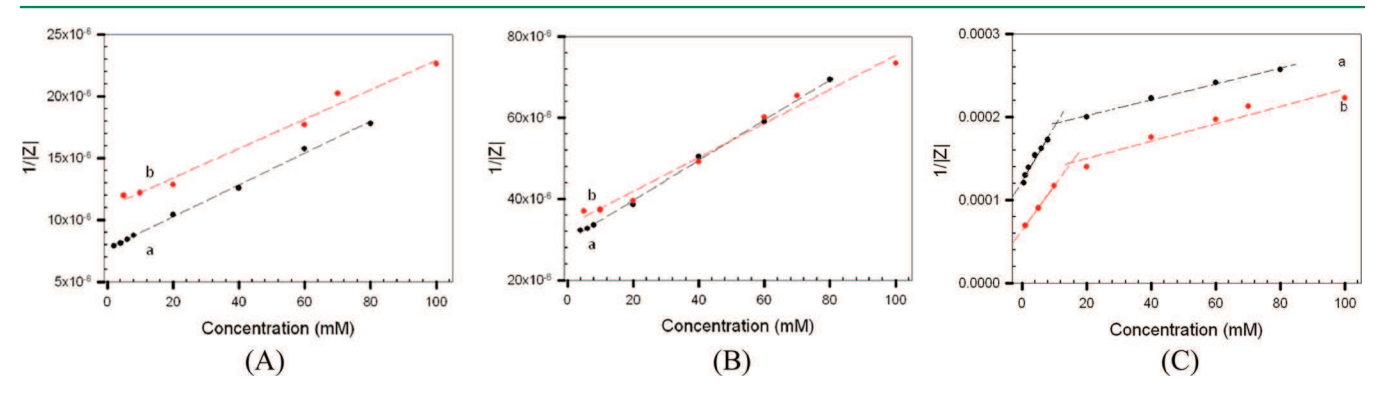


Figure 4. (A, B) Plots of 1/|Z| values obtained from Bode impedance plots at 1 kHz (Figure S3A-B) for MUA-AuNPs/CN/PAN/PET with G-PE on the PET side (A) and the CN side (B) in solutions as a function of K^+ (a) and Na^+ (b) concentration. (C) Plots of 1/|Z| values obtained from Bode impedance plots at 1 kHz (Figure S3C) for PDA-Au NPs (42 nm)/CN/PAN/PET with G-PE in solutions of K^+ (a) and Na^+ (b) as a function of salt concentration.

By extracting the impedance values (|Z|) from Figure 2B in the high frequency region, |Z| is shown to be dependent on the concentration of the ions, especially in the low concentration range. A representative set of 1/IZI vs concentration curves is shown in Figure 3A. In the low concentration range (<20-60 mM), the linear regression slopes of the 1/|Z| vs concentration curves display the order of $K^{+}(3.9 \times 10^{-6}) > Na^{+}(2.3 \times 10^{-6})$ > Li⁺ (1.6 \times 10⁻⁶). The |Z| value becomes smaller when ion concentration increases. In other words, the conductivity increases as the ion concentration increases, and a plateau appears at >60 mM. The slopes are steep when the concentration is <20-60 mM. The nanocomposite membrane appears to be more sensitive to the ions in the lower concentration region. Similar trends are also observed by extracting the charge transfer resistance values from the semicircle fit of Nyquist impedance plots in the high frequency region, as shown in Figure 3B. The magnitudes for the slopes of 1/R vs concentration curves display the order of K⁺ (5.6 \times 10^{-6}) > Na⁺ (4.2 × 10^{-6}) > Li⁺ (2.3 × 10^{-6}), quite similar to those obtained from the data from the Bode impedance plots

These results indicate that the nanocomposite membrane functions as an ion sensitive and selective interfacial scaffold on the interdigitated microelectrode, which is consistent with the cation exchange membrane character of the MUA-Au NP films

embedded in the nanofibrous membrane. In a typical cation-exchange membrane as stationary phase in chromatographic column, the relative affinities of different counterions in the mobile phase depend on the ionic charge, polarizability, and size of the solvated ion, and the type and interaction of the functional groups on the stationary phase. An increase of the charge-density (charge/solvated size) of the ion, or higher charge with smaller solvated ion radius, leads to higher electrostatic interactions with the stationary charges in the membrane (carboxylates), typically $\rm K^+ > Na^+ > Li^+.^{35-41}$ In that case, the ionic conductance of the nanocomposite membranes (1/|Z|) would display the order $\rm K^+ < Na^+ < Li^+$, which is consistent with the experimental observation (Figure 3A).

The same M-Au NPs/CN/PAN/PET scaffold is configured in between a pair of graphite printed electrodes on CN or PET sides of the membrane (Scheme 2B). For example, the impedance responses were measured in the test manifold in which G-PE is on the PET side of the membrane (Scheme 2C). As shown in Bode impedance plots for samples containing Na⁺ (Figure S3A), |Z| value starts to differentiate with various concentrations even in the lower frequency region, and the difference becomes greater in the higher frequency region. Figure 4A shows plots of 1/|Z| values extracted from Bode impedance at 1 kHz vs ionic concentration. In the high frequency region, 1/|Z| shows a clear dependence of the ion

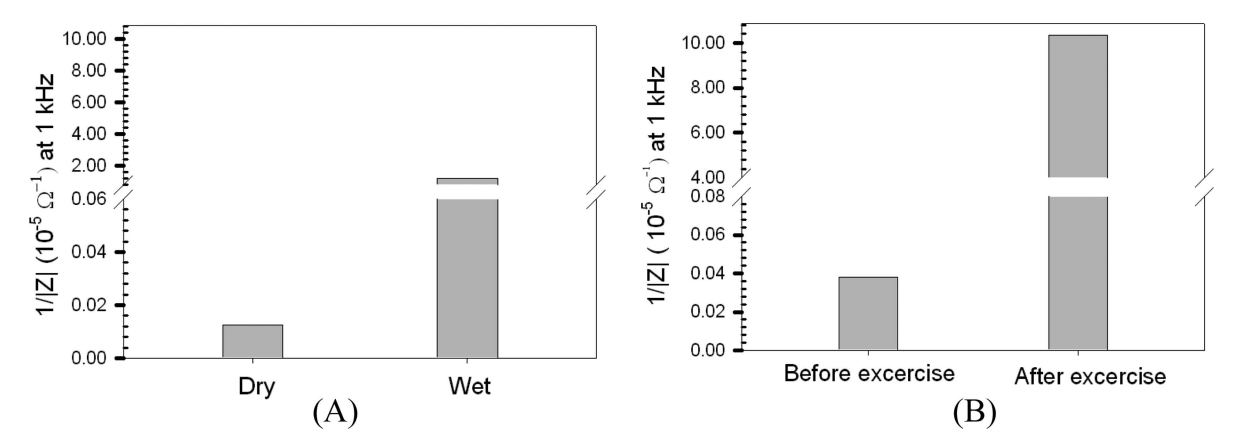


Figure 5. 1/IZI values extracted from Bode impedance plots (Figure S4) for MUA-AuNPs/CN/PAN/PET with G-PE in response to water (as a control, A) and sweat (perspiration test, B). Data were collected by placing a thin nonwoven scaffold on the sensor surface (CN side) and lightly pressing it against the wrist (see Scheme 2D) before and after ~5 min exercise (running stairs). The control experiment was performed by directly placing a drop of water on the dry nanocomposite in between the two electrodes, followed by impedance measurement of the wet membrane.

concentration, similar to the results from NM-Pt-IME device (Figure 3B) except subtle differences in the slope values. The magnitudes for the slopes of 1/|Z| vs concentration curves display the order of K^+ (1.3×10^{-7}) > Na $^+$ (1.2×10^{-7}) in the entire concentration range. A similar trend is also observed by extracting the resistance values from the semicircle fit of Nyquist impedance plots.

For the case of G-PE on the CN side in solutions containing Na⁺ with different concentrations, the |Z| vs frequency curves (Figure S3B) in the low frequency region appear to be independent of the concentration of ions. At > 10 kHz, the impedance shows changes in the |Z| vs frequency curves, exhibiting a clear dependence of the ion concentration. A similar Bode impedance plot is also observed for samples containing K⁺. By extracting the impedance values (|Z|) from the Bode impedance plots at three frequencies in the high frequency region, |Z| is shown to be linearly dependent on the ion concentrations (Figure 4B). The slopes of the 1/IZI vs concentration curves are quite comparable (K^+ (5.0 × 10⁻⁷) ~ Na^+ (4.2 × 10⁻⁷)), showing much smaller differences in comparison with the data shown in Figure 4. A similar trend is also observed by extracting the resistance values from the semicircle fit of Nyquist impedance plots.

The P-NPs/NM scaffolds were also examined. For example, with PDA-Au NPs (42 nm)/CN/PAN/PET being configured in between a printed pair of graphite electrodes on CN or PET sides of the membrane (see Scheme 2B), the Bode impedance plots of solutions containing different concentrations of Na+ show clear changes (Figure S3C). For the data at frequency greater than 10 Hz, bode impedance curves display a clear dependence on the ion concentration. By extracting the impedance values (|Z|) at 1 kHz, a comparison between Na⁺ and K^+ shows that the overall 1/|Z| values of K^+ are greater than those of Na⁺ (Figure 4C). This finding is opposite to the results observed from Au-MUA NPs (see Figure 3), suggesting the operation of a different mechanism in the thin film. In the acrylate-capped Au NPs (42 nm)/CN/PAN/PET membrane, the acrylate-capped Au NPs feature multiple negative charges on the nanoparticle surface. Upon incorporating the positively charged polymer (diallyl ammonium groups), there must be excess negative charges on the NPs which are balanced by the mobile cations in the solution, forming an electrical double layer around the nanoparticles. In this case, it is the ionic

mobility that determines the ionic conductance of the membrane. Since K^+ ions exhibit a higher ionic mobility than Na^+ ions, 42 the overall 1/|Z| values of K^+ are greater than those of Na^+ in the MUA-Au NPs $(7\ nm)/CN/PAN/PET$ membrane. It is important to note that the slopes of the 1/|Z| vs concentration curves are quite comparable between K^+ and Na^+ (e.g., K^+ (6.50 \times 10 $^{-6}$) \sim Na^+ (5.35 \times 10 $^{-6}$) for <20 mM). Unlike MUA-AuNPs film, the selectivity of the PDA-Au NPs film is apparently very limited.

Detection of Sweat. On the basis of the above data for the detection of salts in solutions, the viability of the MUA-AuNPs/ CN/PAN/PET with G-PE on the PET side was further examined with normal volunteers before and after exercises. While sweat contains different chemical constituents with different concentrations, as stated earlier, the study described in this subsection focused on the salt and moisture detections to demonstrate the sensing properties of the as-prepared nanoparticle-nanofibrous nanocomposites. The detection of biological species (e.g., glucose, urea, or lactate) with enzymatic or nonenzymatic modifications of the nanocomposite will be part of our future work. Figure 5 shows a representative set of data with the measurement configuration illustrated in Scheme 2D. The data were extracted from the impedance data (Figure S4) at 1 kHz of volunteers before and after ~5 min exercise (running stairs). The measurement was performed by placing a thin nonwoven scaffold on the sensor surface (CN side) and lightly pressing it against the skin of an individual's wrist, which produces conformal contact between the membrane and volunteer's skin due to the highly flexible and bendable characteristics of the membrane (see Figure S7). The impedance was then monitored before and after exercise or in real time (see Figure S8). A control experiment was also performed by measuring the impedance before and after placing a small drop of pure water onto the sensor surface. In the control experiment, the results clearly show a sharp drop of impedance (or increase of conductance) from dry to wet membrane (Figure 5A). In comparison, the difference between "before exercise" and "after exercise" is much greater than that observed from the control experiment (Figure 5B). This is mainly attributed to the presence of salts in the sweat, which is substantiated by rinsing the membrane with water several times after which the impedance values were almost the same as that before subjecting to sweat test.

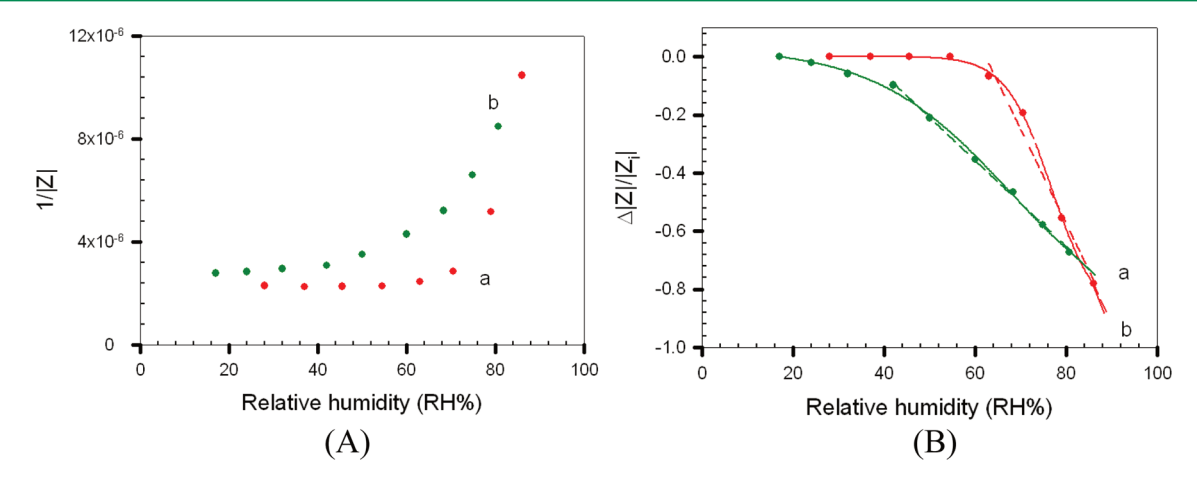


Figure 6. Comparison of 1/|Z| (A) and $\Delta |Z|/|Z_i|$ (B) vs RH% curves (extracted from Bode impedance plots at 20 kHz) as a function of relative humidity for two different sensing scaffolds: MUA-Au NPs (7 nm) NM (slope in linear region: -3.2×10^{-2} (a)) and PDA-Au NPs (70 nm) NM (slope in linear region: -1.5×10^{-2} (b)).

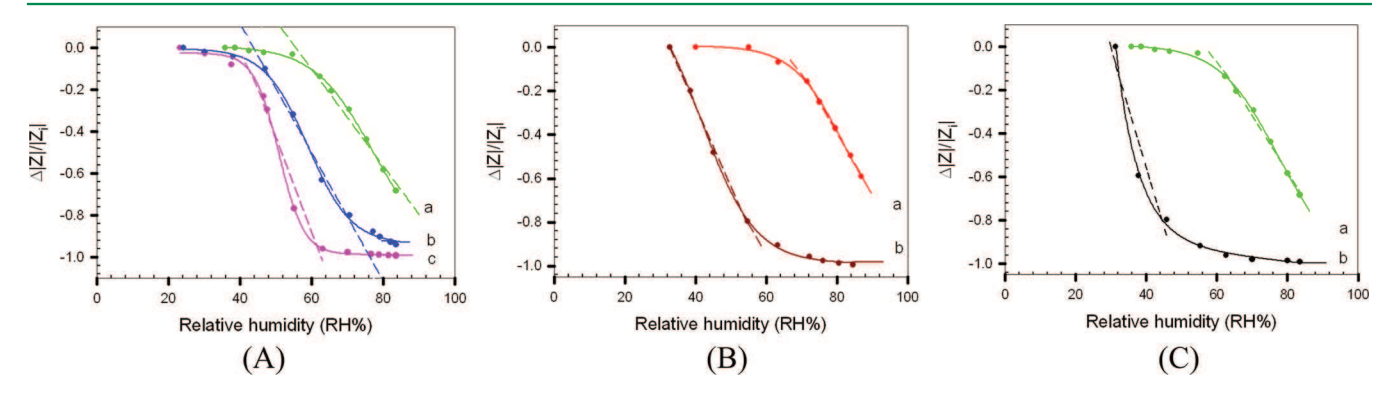


Figure 7. Plots of $\Delta |Z|/|Z_i|$ vs RH% for PDA-AuNPs/CN/PAN/PET NM on Pt-IME. (A) Data for scaffolds derived from PDA of constant concentration and Au NPs (70 nm) of different concentrations (5.0 × 10^{10} (a), 2.0 × 10^{11} (b), and 1.0 × 10^{11} NPs/mL (c)). (B) Data for scaffolds derived from PDA with different concentrations (0.4 M (a) and 0.76 M (b)) and the same concentration of Au NPs (70 nm, 5.0 × 10^{10} NPs/mL). (Slopes: (A) -2.3×10^{-2} (a); -2.0×10^{-2} (b); and -4.5×10^{-2} (c); and (B) -2.8×10^{-2} (a); and -3.1×10^{-2} (b)). (C) Data for scaffolds derived from PDA of the same concentration (0.4 M) and Au NPs of two different sizes (70 nm (a) and 42 nm (b)). (Slopes: -2.6×10^{-2} (a) and -3.6×10^{-2} (b).)

It is evident that the relative change for the individual before and after exercise (96%) is smaller than that for the control experiment using pure water (99%). This is expected because salts in the sweat greatly increase the conductivity in comparison with pure water.

Detection of Relative Humidity Changes in Air and from Perspiration. Detection of Relative Humidity Changes in Air. With devices of Au_{70 nm}/CN/PAN/PET (with G-PE on CN side), the response characteristics between PDA-Au NPs (70 nm) and MUA-Au NPs (7 nm) in NM were first compared. The impedance data at different RH% were collected by flowing air or N2 from a water bubbler with a flow controller, at each flow rate the RH% were recorded by a commercial humidity meter. Data were first obtained with a sensor device of MUA-Au NPs/CN/PAN/PET on G-PE in which the G-PE is on CN side. On the basis of impedance data extracted from Bode impedance plots, both 1/IZI (Figure 6A) and $\Delta |Z|/|Z_i|$ (= $(|Z| - |Z_i|)/|Z_i|$ where Z_i is the initial impedance) (Figure 6B) are plotted against RH%, in which the $\Delta |Z|/|Z_i| \sim RH\%$ plots seem to provide a better comparison of the responses. When RH% > 50%, the results display a significant response. When RH% < 50%, the response is independent of RH%. The results are likely reflecting the low hydrophilicity of the nanocomposite membrane, which is

responsible for the insignificant response sensitivity in the low RH% range.

To manipulate the hydrophilicity, a highly hydrophilic polymer, PDA, was used for the assembly of Au NPs in the nanocomposite membrane. The membranes were fabricated by PDA mediated assembly of acrylate-capped Au NPs of different sizes (70 or 42 nm) in the nanofibrous membranes. Different concentration ratios of PDA vs Au NPs were studied for the assemblies. As shown in Figure 6B for PDA-Au NPs (70 nm)/ CN/PAN/PET NM on G-PE, it is evident that the response to a wider RH% range. Note that the slope in the low RH% range (<50%) is slightly smaller than that in the high RH% range. In comparison with MUA-Au NPs/CN/PAN/PET on G-PE, in the high RH% range (>50%), the sensitivity of PDA-Au NPs (70 nm)/CN/PAN/PET NM on G-PE is relatively smaller, indicating the importance of balancing hydrophobicity and hydrophilicity in the nanocomposite. Note that the sensitivity also depends on the gap between electrodes. A smaller gap shows a great sensitivity, which is evidenced by the impedance changes as a function of relative humidity for PDA-Au NPs (70 nm)/CN/PAN/PET NM with G-PE with different G-electrode gaps. In this work, no attempt was made to maximize the sensitivity by further reducing the electrode gap.

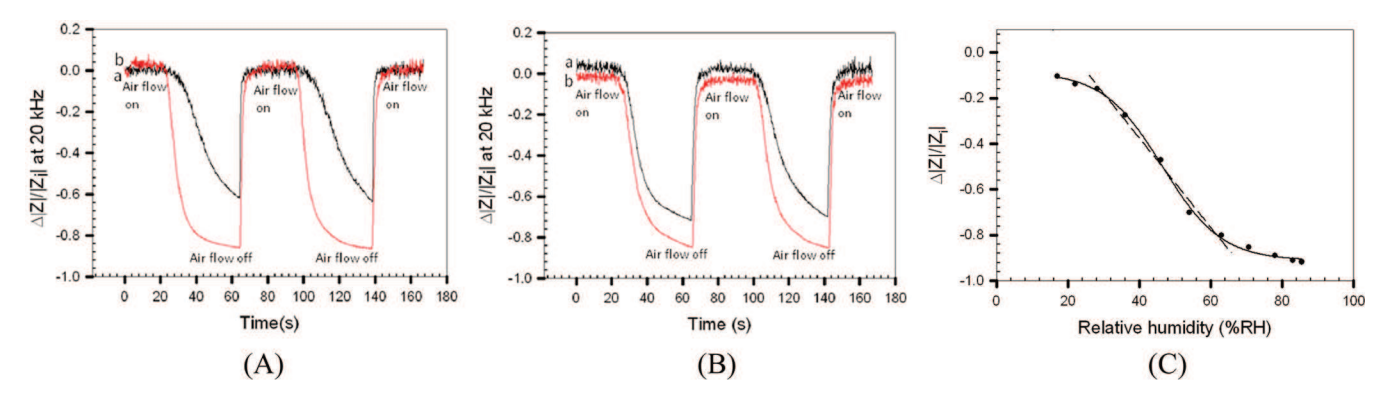


Figure 8. (A,B) Sensor responses ($\Delta |Z|/|Z_i|$) measured at ~20 kHz for a device of PDA-AuNPs (70 nm)/CN/PAN/PET with G-PE for two volunteers (#1 (A) and #2 (B)) before (a) and after (b) exercise (running stairs for ~5 min). The measurement was performed by placing the sensor compartment on the palm and the perspiration was measured by stopped air flow method (see Scheme 2E). (C) Calibration curve for the same sensor device with controlled RH% in air (slope: 2.0×10^{-2}).

To understand the composition effect of the nanocomposite on response characteristics, we also examined the nanocomposite membranes with different ratios of Au NPs vs PDA, as well as different particle sizes using IME as the detection platform. With PDA-Au NPs (70 nm)/CN/PAN/ PET on Pt-IME (Scheme 2A) placed in the test manifold (Scheme 2C), a series of impedance values (|Z|) extracted from the Bode impedance plots at 20 kHz (not shown) as a function of the relative humidity are compared with sensors of PDA-Au NPs/CN/PAN/PET on Pt-IME with subtle differences in PDA and Au NPs. Figure 7A shows a set of $\Delta Z/Z_i$ data (also see Figure S5A) as a function of the relative humidity for PDA-Au NPs/CN/PAN/PET prepared by mixing PDA with a constant concentration and Au NPs (70 nm) with different concentrations. It is evident that both the sensitivity and the sensitive range increase with an increase ratio of Au NPs to PDA in the NM. Figure 7B shows a set of $\Delta Z/Z_i$ data (also see Figure S5B) as a function of relative humidity for PDA-Au NPs/CN/PAN/ PET prepared by mixing Au NPs with a constant concentration and PDA of different concentrations. The sensitivity in the low RH% range increases with PDA concentration in the NM. However, in the high RH% range the sensitivity increases with a decrease of PDA concentration in the NM. This behavior is consistent with the highly hydrophilic nature of PDA.

The particle size effect on the response sensitivity was also examined. Figure 7C shows a set of $\Delta Z/Z_i$ data as a function of relative humidity for PDA-Au NPs/CN/PAN/PET NM/G-PE with Au NPs of two different sizes. It is evident that the NM with small size Au NPs seems to exhibit overall smaller 1/|Z| value in comparison with the large size NPs (see Figure SSC). The sensitivity clearly depends on the particle size in different RH% ranges. The smaller-sized particles show a higher sensitivity in the low RH% region, whereas the larger-sized particles exhibit a higher sensitivity in the high RH% region.

Detection of Perspiration. The viability of PDA-AuNPs/CN/PAN/PET devices (with G-PE) for detection of perspiration was examined with normal individual volunteers before and after exercises. Figure 8 shows a typical set of $\Delta Z/Z_i$ response (measured at \sim 20 kHz) of a device of PDA-AuNPs/CN/PAN/PET (with G-PE on CN side) with the measurement configuration illustrated in Scheme 2E. Data were collected from palms of volunteers #1 and #2 before and after \sim 5 min exercise (running stairs). The measurement was performed by placing the sensor compartment on top of the palm and the perspiration was measured by stopped air flow

method.¹ During the initial 30 s, air flows into the device to establish a baseline. The perspiration of the volunteer's palm was monitored for 45 s upon stopping air flow. The baseline returns upon air flowing again. This procedure was repeated for one more time. The responses to exercises are significant and reversible, with the response magnitude being clearly dependent on the individual, as reflected by the difference between #1 and #2.

Based on the relative changes of $\Delta Z/Z_i$ values before and after the exercises, it is evident that the corresponding changes of RH% falls in between 50 and 72% (for #1) and 56–62% (for #2), as estimated from the calibration data shown in Figure 8C.

Devices with G-PE on the PET side were also tested. For example, the response for PDA-AuNPs/CN/PAN/PET with G-PE on the PET side was found to be much smaller than that with G-PE on the CN side. This finding is indicative of the importance of the nanocomposite membrane-electrode configuration in the sensor response.

CONCLUSION

In conclusion, a novel class of nanocomposite membranes has been demonstrated for constructing sensitive scaffolds for potential applications in flexible sweat sensors. The nanocomposites are assembled by molecular or polymeric linkers that incorporate gold nanoparticles into a three-layer structured nanofibrous membrane. Impedance measurements of the nanocomposite membrane as a scaffold of chemiresistor-type platform have demonstrated the capabilities for ion detection in solutions with dissolved salts and changes of relative humidity in the atmosphere. This nanoparticle-nanofiber sensor platform is further demonstrated as a flexible sensor strip for detecting changes in sweating and perspiration of individuals before and after exercises, showing promising potentials for applications of the flexible nanocomposite scaffolds in wearable sweat sensors. Further refinements of the nanocomposite structures with functionalized or alloyed gold nanoparticles and surface-modified nanofibrous membranes in our ongoing work is expected to enhance the performance characteristics of the flexible sensors toward the targeted applications.

ASSOCIATED CONTENT

S Supporting Information

The Supporting Information is available free of charge on the ACS Publications website at DOI: 10.1021/acssensors.6b00414.

TEM images of Au NPs, SEM images of nanofibrous membranes and nanoparticle—nanofibrous nanocomposite membranes, schemes illustrating the equivalent circuits of the device, Bode impedance plots of ions in different nanocomposite, 1/IZI vs RH% plots extracted from Bode impedance, photos showing the sensor setups for perspiration and sweat detection, and photos showing the flexible bending of the nanofibrous membrane (PDF)

AUTHOR INFORMATION

Corresponding Author

*E-mail: cjzhong@binghamton.edu.

Notes

The authors declare no competing financial interest.

ACKNOWLEDGMENTS

Financial support of this work from SUNY Network of Excellence Fund, and in part from NSF (IIP 1640669), is gratefully acknowledged.

REFERENCES

- (1) Chang, B. W.; Yeh, S. J.; Tsai, P. P.; Chang, H. C. Monitoring perspiration from palms of hypohidrosis patients with a stopped-flow conductometric mini-system. *Clin. Chim. Acta* **2004**, 348, 107–111.
- (2) Indo, Y.; Tsuruta, M.; Hayashida, Y.; Karim, M. A.; Ohta, K.; Kawano, T.; Mitsubuchi, H.; Tonoki, H.; Awaya, Y.; Matsuda, I. Mutations in the TRKA/NGF receptor gene in patients with congenital insensitivity to pain with anhidrosis. *Nat. Genet.* **1996**, *13*, 485–488.
- (3) Eisenach, J. H.; Atkinson, J. L. D.; Fealey, R. D. Hyperhidrosis: Evolving Therapies for a Well-Established Phenomenon. *Mayo Clin. Proc.* **2005**, *80*, 657–666.
- (4) Lao, L. M.; Kumakiri, M.; Mima, H.; Kuwahara, H.; Ishida, H.; Ishiguro, K.; Fujita, T.; Ueda, K. The ultrastructural characteristics of eccrine sweat glands in a Fabry disease patient with hypohidrosis. *J. Dermatol. Sci.* **1998**, *18*, 109–117.
- (5) Morgan, R. M.; Patterson, M. J.; Nimmo, M. A. Acute effects of dehydration on sweat composition in men during prolonged exercise in the heat. *Acta Physiol. Scand.* **2004**, *182*, 37–43.
- (6) Al-Omari, M.; Sel, K.; Mueller, A.; Edwards, J.; Kaya, T. Detection of relative [Na⁺] and [K⁺] levels in sweat with optical measurements. *J. Appl. Phys.* **2014**, *115*, 203107.
- (7) Lee, J.; Pyo, M.; Lee, S. H.; Kim, J.; Ra, M.; Kim, W. Y.; Park, B. J.; Lee, C. W.; Kim, J. M. Hydrochromic conjugated polymers for human sweat pore mapping. *Nat. Commun.* **2014**, *5*, 1–10.
- (8) Gao, W.; Emaminejad, S.; Nyein, H. Y.; Challa, S.; Chen, K.; Peck, A.; Fahad, H. M.; Ota, H.; Shiraki, H.; Kiriya, D.; Lien, D. H.; Brooks, G. A.; Davis, R. W.; Javey, A. Fully integrated wearable sensor arrays for multiplexed in situ perspiration analysis. *Nature* **2016**, 529, 509–514.
- (9) Mahfouz, M. R.; Kuhn, M. J.; To, G. Wireless medical devices: A review of current research and commercial systems. In *Biomedical Wireless Technologies, Networks, and Sensing Systems (BioWireleSS)*; IEEE Topical Conference; IEEE: New York, **2013**, pp 16–18.10.1109/BioWireleSS.2013.6613660
- (10) Schazmann, B.; Morris, D.; Slater, C.; Beirne, S.; Fay, C.; Reuveny, R.; Moyna, N.; Diamond, D. A wearable electrochemical sensor for the real-time measurement of sweat sodium concentration. *Anal. Methods* **2010**, *2*, 342–348.
- (11) Bandodkar, A. J.; Hung, V. W.; Jia, W.; Valdés-Ramírez, G.; Windmiller, J. R.; Martinez, A. G.; Ramírez, J.; Chan, G.; Kerman, K.; Wang, J. Tattoo-based potentiometric ion-selective sensors for epidermal pH monitoring. *Analyst* **2013**, *138*, 123–128.
- (12) Curto, V. F.; Fay, C.; Coyle, S.; Byrne, R.; O'Toole, C.; Barry, C.; Hughes, S.; Moyna, N.; Diamond, D.; Benito-Lopez, F. Real-time sweat pH monitoring based on a wearable chemical barcode micro-

fluidic platform incorporating ionic liquids. Sens. Actuators, B 2012, 171, 1327-1334.

- (13) Kim, J.; de Araujo, W. R.; Samek, I. A.; Bandodkar, A. J.; Jia, W.; Brunetti, B.; Paixão, T. R.; Wang, J. Wearable temporary tattoo sensor for real-time trace metal monitoring in human sweat. *Electrochem. Commun.* **2015**, *51*, 41–45.
- (14) Bandodkar, A. J.; Molinnus, D.; Mirza, O.; Guinovart, T.; Windmiller, J. R.; Valdés-Ramírez, G.; Andrade, F. J.; Schöning, M. J.; Wang, J. Epidermal tattoo potentiometric sodium sensors with wireless signal transduction for continuous non-invasive sweat monitoring. *Biosens. Bioelectron.* **2014**, *54*, 603–609.
- (15) Curto, V. F.; Coyle, S.; Byrne, R.; Angelov, N.; Diamond, D.; Benito-Lopez, F. Concept and development of an autonomous wearable micro-fluidic platform for real time pH sweat analysis. *Sens. Actuators, B* **2012**, *175*, 263–270.
- (16) Guinovart, T.; Bandodkar, A. J.; Windmiller, J. R.; Andrade, F. J.; Wang, J. A potentiometric tattoo sensor for monitoring ammonium in sweat. *Analyst* **2013**, *138*, 7031–7038.
- (17) Al-Omari, M.; Sel, K.; Mueller, A.; Edwards, J.; Kaya, T. Detection of relative [Na⁺] and [K⁺] levels in sweat with optical measurements. *J. Appl. Phys.* **2014**, *115*, 203107.
- (18) Schittek, B.; Hipfel, R.; Sauer, B.; Bauer, J.; Kalbacher, H.; Stevanovic, S.; Schirle, M.; Schroeder, K.; Blin, N.; Meier, F.; Rassner, G.; Garbe, C. Dermcidin: a novel human antibiotic peptide secreted by sweat glands. *Nat. Immunol.* **2001**, *2*, 1133–1137.
- (19) Sonner, Z.; Wilder, E.; Heikenfeld, J.; Kasting, G.; Beyette, F.; Swaile, D.; Sherman, F.; Joyce, J.; Hagen, J.; Kelley-Loughnane, N.; Naik, R. The microfluidics of the eccrine sweat gland, including biomarker partitioning, transport, and biosensing implications. *Biomicrofluidics* **2015**, *9*, 031301.
- (20) Khodagholy, D.; Curto, V. F.; Fraser, K. J.; Gurfinkel, M.; Byrne, R.; Diamond, D.; Malliaras, G. G.; Benito-Lopez, F.; Owens, R. M. Organic electrochemical transistor incorporating an ionogel as a solid state electrolyte for lactate sensing. *J. Mater. Chem.* **2012**, 22, 4440–4443.
- (21) Corrie, S. R.; Coffey, J. W.; Islam, J.; Markey, K. A.; Kendall, M. A. F. Blood, sweat, and tears: developing clinically relevant protein biosensors for integrated body fluid analysis. *Analyst* **2015**, *140*, 4350–4364
- (22) Matzeu, G.; Florea, L.; Diamond, D. Advances in wearable chemical sensor design for monitoring biological fluids. *Sens. Actuators, B* **2015**, *211*, 403–418.
- (23) Ma, H.; Burger, C.; Hsiao, B. S.; Chu, B. Ultrafine polysaccharide nanofibrous membranes for water purification. *Biomacromolecules* **2011**, *12*, 970–976.
- (24) Ma, H.; Hsiao, B. S.; Chu, B. Thin-film nanofibrous composite membranes containing cellulose or chitin barrier layers fabricated by ionic liquids. *Polymer* **2011**, *52*, 2594–2599.
- (25) Wang, X.; Fang, D.; Hsiao, B. S.; Chu, B. Nanofiltration membranes based on thin-film nanofibrous composites. *J. Membr. Sci.* **2014**, *469*, 188–197.
- (26) Zhao, W.; Al-Nasser, L. F.; Shan, S.; Li, J.; Skeete, Z.; Kang, N.; Luo, J.; Lu, S.; Zhong, C. J.; Grausgruber, C. J.; Harris, R. Detection of mixed volatile organic compounds and lung cancer breaths using chemiresistor arrays with crosslinked nanoparticle thin films. *Sens. Actuators, B* **2016**, 232, 292–299.
- (27) Zhao, W.; Luo, J.; Shan, S.; Lombardi, J. P.; Xu, Y.; Cartwright, K.; Lu, S.; Poliks, M.; Zhong, C. J. Sensors: Nanoparticle-Structured Highly Sensitive and Anisotropic Gauge Sensors. *Small* **2015**, *11*, 4508–4508.
- (28) Zhao, W.; Rovere, T.; Weerawarne, D.; Osterhoudt, G.; Kang, N.; Joseph, P.; Luo, J.; Shim, B.; Poliks, M.; Zhong, C. J. Nanoalloy Printed and Pulse-Laser Sintered Flexible Sensor Devices with Enhanced Stability and Materials Compatibility. ACS Nano 2015, 9, 6168–6177.
- (29) Shan, S.; Zhao, W.; Luo, J.; Yin, J.; Switzer, J. C.; Joseph, P.; Lu, S.; Poliks, M.; Zhong, C. J. Flexibility characteristics of a polyethylene terephthalate chemiresistor coated with a nanoparticle thin film assembly. *J. Mater. Chem. C* **2014**, *2*, 1893–1903.

(30) Brust, M.; Walker, M.; Bethell, D.; Schiffrin, D. J.; Whyman, R. Synthesis of thiol-derivatised gold nanoparticles in a two-phase liquid—liquid system. *J. Chem. Soc., Chem. Commun.* **1994**, *7*, 801—802.

- (31) Hostetler, M. J.; Wingate, J. E.; Zhong, C. J.; Harris, J. E.; Vachet, R. W.; Clark, M. R.; Londono, J. D.; Green, S. J.; Stokes, J. J.; Wignall, G. D.; Glish, G. L.; et al. Alkanethiolate gold cluster molecules with core diameters from 1.5 to 5.2 nm: core and monolayer properties as a function of core size. *Langmuir* 1998, 14, 17–30.
- (32) Maye, M. M.; Zheng, W.; Leibowitz, F. L.; Ly, N. K.; Zhong, C. J. Heating-induced evolution of thiolate-encapsulated gold nanoparticles: a strategy for size and shape manipulation. *Langmuir* **2000**, *16*, 490–497.
- (33) Han, L.; Luo, J.; Kariuki, N. N.; Maye, M. M.; Jones, V. W.; Zhong, C. J. Novel interparticle spatial properties of hydrogen-bonding mediated nanoparticle assembly. *Chem. Mater.* **2003**, *15*, 29–37
- (34) Njoki, P. N.; Lim, I. I. S.; Mott, D.; Park, H. Y.; Khan, B.; Mishra, S.; Sujakumar, R.; Luo, J.; Zhong, C. J. Size correlation of optical and spectroscopic properties for gold nanoparticles. *J. Phys. Chem. C* **2007**, *111*, 14664–14669.
- (35) Teesch, L. M.; Adams, J. Fragmentations of gas-phase complexes between alkali metal ions and peptides: metal ion binding to carbonyl oxygens and other neutral functional groups. *J. Am. Chem. Soc.* 1991, 113, 812–820.
- (36) Cheung, R. C. F.; Wong, J. H.; Ng, T. B. Immobilized metal ion affinity chromatography: a review on its applications. *Appl. Microbiol. Biotechnol.* **2012**, *96*, 1411–1420.
- (37) Chaga, G. S. Twenty-five years of immobilized metal ion affinity chromatography: past, present and future. *J. Biochem. Biophys. Methods* **2001**, *49*, 313–334.
- (38) Gaberc-Porekar, V.; Menart, V. Perspectives of immobilized-metal affinity chromatography. *J. Biochem. Biophys. Methods* **2001**, 49, 335–360.
- (39) Marino, T.; Russo, N.; Toscano, M. Interaction of Li⁺, Na⁺, and K⁺ with the proline amino acid. Complexation modes, potential energy profiles, and metal ion affinities. *J. Phys. Chem. B* **2003**, *107*, 2588–2594
- (40) Remko, M.; Rode, B. M. Effect of metal ions (Li⁺, Na⁺, K⁺, Mg²⁺, Ca²⁺, Ni²⁺, Cu²⁺, and Zn²⁺) and water coordination on the structure of glycine and zwitterionic glycine. *J. Phys. Chem. A* **2006**, *110*, 1960–1967.
- (41) Cerda, B. A.; Wesdemiotis, C. Li⁺, Na⁺, and K⁺ binding to the DNA and RNA nucleobases. Bond energies and attachment sites from the dissociation of metal ion-bound heterodimers. *J. Am. Chem. Soc.* **1996**, *118*, 11884–11892.
- (42) Lee, S. H.; Rasaiah, J. C. Molecular dynamics simulation of ionic mobility. I. Alkali metal cations in water at 25°C. *J. Chem. Phys.* **1994**, *101*, 6964–6974.